Biophysical Journal
Article

Biophysical Society

Microfluidic measurement of the size and shape of lipid-anchored proteins

Sreeja Sasidharan,[1] Leah Knepper,[2] Emily Ankrom,[2] Gabriel Cucé,[1] Lingyang Kong,[3] Amanda Ratajczak,[1] Wonpil Im,[3] Damien Thévenin,[2] and Aurelia Honerkamp-Smith[1,*]
[1]Department of Physics, Lehigh University, Bethlehem, Pennsylvania; [2]Department of Chemistry, Lehigh University, Bethlehem, Pennsylvania; and [3]Department of Biological Sciences, Lehigh University, Bethlehem, Pennsylvania

ABSTRACT The surface of a cell is crowded with membrane proteins. The size, shape, density, and mobility of extracellular surface proteins mediate cell surface accessibility to external molecules, viral particles, and other cells. However, predicting these qualities is not always straightforward, even when protein structures are known. We previously developed an experimental method for measuring flow-driven lateral transport of neutravidin bound to biotinylated lipids in supported lipid bilayers. Here, we use this method to detect hydrodynamic force applied to a series of lipid-anchored proteins with increasing size. We find that the measured force reflects both protein size and shape, making it possible to distinguish these features of intact, folded proteins in their undisturbed orientation and proximity to the lipid membrane. In addition, our results demonstrate that individual proteins are transported large distances by flow forces on the order of femtoNewtons, similar in magnitude to the shear forces resulting from blood circulation or from the swimming motion of microorganisms. Similar protein transport across living cells by hydrodynamic force may contribute to biological flow sensing.

SIGNIFICANCE Peripheral membrane proteins attached to the membrane by a lipid anchor are easily moved across the membrane by flows in the surrounding fluid. We measured the hydrodynamic force applied to individual proteins attached to a lipid bilayer using fluorescence microscopy. By observing lateral movement of differently sized proteins in a simplified model membrane system, we show how flow-driven transport depends on protein size and shape. We show that membrane proteins can be spatially organized by small forces similar to those resulting from circulatory flow in blood vessels. Using microfluidic flow to organize proteins makes it possible to measure forces with sub-femtoNewton precision; the forces applied by shear stress are 10–100 times smaller than forces applied by thermal energy, by individual molecular motors, or in single-molecule force spectroscopy experiments.

INTRODUCTION

The outer surface of mammalian cells displays a diverse array of peripheral and integral membrane proteins. Glycosylphosphatidylinositol anchors serve both to anchor soluble proteins to the lipid bilayer and locate them on its extracellular face. Extracellular glycosylphosphatidylinositol-anchored proteins mediate many crucial physiological processes, such as immune function regulation (1), sperm cell entry to an egg (2), and directional cell migration (3). The size, density, and chemistry of surface proteins modify the accessibility of the cell surface. In some cases, surface proteins create a substantial physical barrier to the membrane. For example, endothelial cells lining the inner surface of blood vessels are covered by a glycocalyx, which consists of membrane-anchored proteoglycans and secreted polysaccharides and can be several hundreds of nanometers thick (4,5). Reduced glycocalyx thickness is associated with disease processes including atherosclerosis and sepsis (6,7). Surface protein size and crowding also impact other critical physiological events: for instance, viral fusion glycoproteins must bring the cell and enveloped virus membranes close together to achieve membrane fusion.

To understand how cell surface proteins affect these interactions, it is necessary to consider the size and shape of membrane molecules in situ, preserving their position relative to the membrane. However, this information is lost when proteins are isolated from membranes for crystallization. Glycocalyx proteins such as glypican-1 are attached to their lipid anchor by a long, unstructured linker and also

Submitted April 8, 2024, and accepted for publication August 29, 2024.
*Correspondence: auh216@lehigh.edu
Editor: Ilya Levental.
https://doi.org/10.1016/j.bpj.2024.08.026

bear multiple flexible polysaccharide chains, leading to a large range of possible configurations (8). In addition, surface protein density impacts the configuration of lengthy polysaccharides: surface-attached polymers can adopt either a "polymer brush" configuration at high density or a "mushroom" configuration at lower density.

Common biochemical methods for separating mixtures of proteins rely on electrophoresis and sort denatured proteins according to their net charge or molecular weight. However, when proteins are denatured, information about the three-dimensional tertiary structure of the folded protein is lost. While precise protein structure is accessible via crystallography, the protein must be first isolated from its environment. Cryoelectron microscopy techniques can image proteins embedded in their native membranes (9,10), but these experiments require frozen samples. Dynamic information about membrane protein conformation relative to the membrane is challenging to obtain.

Recently, a separation method specific to membrane proteins has been developed: using electrophoresis or flow to move intact proteins across the surface of a solid-supported lipid bilayer. Groves and Boxer demonstrated electrophoresis of fluorescent lipids within supported membranes in 1995 (11), while more recent experiments have used electric fields to separate membrane proteins and charged lipids (12,13). Shear-driven motion of lipid-anchored proteins has been observed on the surface of swimming organisms and during in vitro experiments (14–16). Flow separation of proteins depends on the shape and size of the protein's aqueous region, and on the drag applied by the membrane. This tactic has been most frequently applied to proteins anchored to the membrane by a lipid molecule. Jönsson et al. demonstrated separation of labeled lipids and membrane-anchored proteins attached to a lipid bilayer flowing along the lower surface of microfluidic channels (15). Hu et al. modified this method to characterize flow forces on a series of lipids and lipid-anchored proteins (17).

We previously demonstrated an experimental method to measure the advective mobility of neutravidin proteins bound to isolated patches of supported lipid bilayer containing biotinylated lipids (Fig. 1, *A* and *B*) (18). This method has the advantage that low shear stress is applied, so the membrane stays in place and only proteins are transported. We showed that our method is sensitive enough to distinguish differences in flow mobility for the same protein in membranes with different viscosities. Our previous experiments were limited by uncertainty about the number of lipid anchors attached to each neutravidin molecule (four biotin binding sites are available). Fortunately, in 2012, Lim et al. designed and engineered a stable streptavidin monomer with a single, functional biotin binding site, using substitution of binding site residues from rhizavidin, a monomeric biotin binding protein originating in the root nodule bacterium *Rhizobium etli* (19). Here, we use this monomer as the basis for a series of constructs with different sizes, each of which can bind only a single biotinylated lipid: monomeric streptavidin (mSA), monomeric streptavidin conjugated to enhanced green fluorescent protein (mSA-GFP), and monomeric streptavidin conjugated to maltose binding protein (mSA-MBP), (Fig. 1 *C*). We use microfluidics and fluorescence microscopy to compare flow-driven transport of these constructs with that of commercially available streptavidin (SA). While applying physiologically relevant levels of shear stress, we show that we can measure hydrodynamic force with enough precision to distinguish between lipid-anchored proteins with similar molecular weights but different shapes. We conducted an all-atom molecular dynamics simulation to choose an appropriate geometric approximation for our proteins, and we use this approximation to generate quantitative estimates of protein size and shape using our measurements of flow transport.

MATERIALS AND METHODS

Fusion protein expression plasmids

The plasmids pET-mSA-MBP (Addgene, Watertown, MA, no. 52319) and pRSET-mSA-EGFP (Addgene, no. 39862) (19) were transformed into

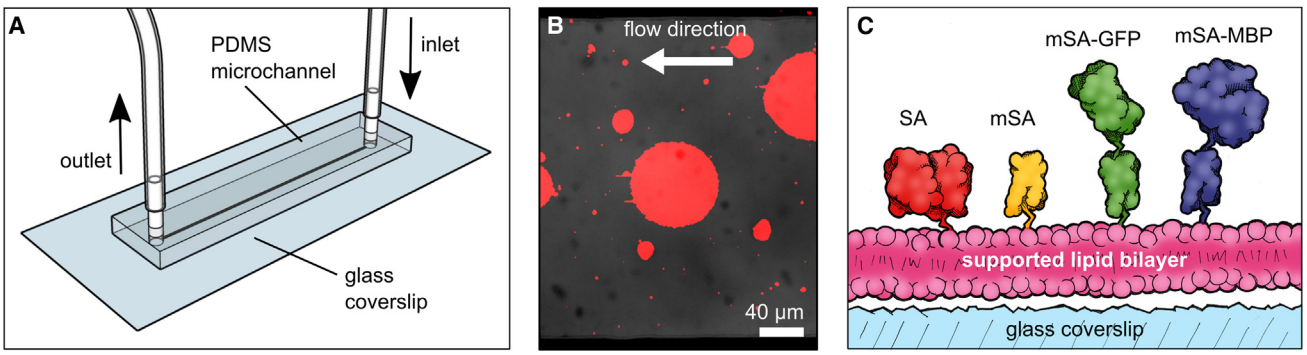

FIGURE 1 Microfluidic apparatus and proteins. (*A*) Schematic showing rectangular microfluidic channel with tubing connections. (*B*) Overlay of fluorescence and bright-field images showing supported lipid bilayer patches labeled with TXRed-DPPE. (*C*) Illustration of the series of lipid-anchored proteins used in our experiments. Streptavidin (SA) was obtained commercially, while monomeric streptavidin (mSA), mSA-GFP, and mSA-MBP were expressed, purified, and labeled as described in the materials and methods.

Rosetta (DE3) BL21. A 5 mL overnight culture in Lennox broth (LB) was used to inoculate 250 mL LB with 100 μg/mL ampicillin. We modeled our purification scheme using previously described protocols for SA monomer purification (20). The culture was incubated at 37°C on an orbital shaker (200 rpm) until an OD_{600} of 0.9, when it was induced with isopropyl β-D-1-thiogalactopyranoside: 500 μM for mSA-MBP and 100 μM for mSA-GFP. Induced cultures grew at 37°C for 4 h with shaking before harvesting by centrifugation at 10,000 rpm, 4°C for 15 min.

Purification and refolding of mSA-GFP

The cell pellet was processed to isolate mSA-EGFP inclusion bodies. Cells were lysed at 4°C by probe sonication with a Branson Sonifier 450 in buffer 1 (50 mM NaH_2 PO_4, 300 mM NaCl [pH 8.0]) containing 1 mM phenylmethylsulfonyl fluoride for 10 min (duty cycle, 30%; output control, 2) and centrifuged for 10 min at 12,500 × g. The resulting pellet was resuspended in 15 mL buffer 1 containing 1% Triton X-100 and 1 M urea (buffer 2) and incubated on ice for 10 min. The sample was then centrifuged for 10 min at 12,500 × g, and the resulting pellet was washed twice with 10–15 mL of buffer 2. Lastly, the pellet containing mSA-GFP inclusion bodies was washed with 30 mL of buffer 1 to remove detergent. mSA-GFP inclusion bodies were solubilized using 10 mL of 8 M urea in buffer 1 (buffer 3) for approximately 16 h at 4°C under rotation. The insoluble fraction was removed by centrifugation for 15 min at 12,500 × g, and the supernatant was filtered sequentially through 0.45 μm PVDF and 0.22 μm PES (Thermo Fisher Scientific, Hampton, NH) syringe filters. The filtrate was incubated with 3 mL HisPur Ni-NTA resin (Thermo Fisher Scientific) for 2 h at 4°C under rotation. The protein was purified using a gravity flow column by first washing the resin 3–4 times with buffer 3 containing 25 mM imidazole before elution with at least 2 column volumes of buffer 3 containing 300 mM imidazole. Purified mSA-GFP was concentrated to 1–2 mL using a 10 kDa MWCO Amicon Ultra Centrifugal Filter (MilliporeSigma, Burlington, VT) and added dropwise to 50 mL ice-cold refolding buffer under rapid stirring at 4°C (refolding buffer: buffer 1 containing 0.3 mg/mL biotin, 0.2 mg/mL oxidized glutathione, 1 mg/mL reduced glutathione). The protein was refolded under stirring over 24 h at 4°C. Refolded mSA-GFP was centrifuged to remove precipitates and concentrated to approximately 1 mL using a 10 kDA centrifuge concentrator. Residual biotin was removed by dialyzing the protein for 4 h at 37°C against buffer 1 before exchanging the buffer and dialyzing overnight at 4°C. mSA-GFP was lastly subjected to size-exclusion chromatography using a HiPrep 16/60 Sephacryl S-300 HR column (Cytiva, Marlborough, MA) to separate aggregates and buffer exchange the protein into 50 mM NaH_2 PO_4 with 150 mM NaCl. Purity was evaluated by SDS-PAGE followed by Coomassie staining (Fig. S1).

Purification of mSA-MBP

Cell pellets were resuspended in 50 mM $NaPO_4$ and 300 mM NaCl (pH 8.0) and lysed by sonication at 4°C for 10 min (duty cycle, 30%; output control, 2) before centrifugation at 12,500 rpm, 4°C for 30 min. The supernatant (containing soluble protein) was filtered with a 0.45 μm PVDF filter and then incubated with HisPur Ni-NTA resin under rotation for 1 h at 4°C. The flow-through was re-applied to the column (no second incubation) before washing with 50 mM $NaPO_4$, 300 mM NaCl, and 20 mM imidazole (pH 8.0). The protein of interest was eluted with 50 mM $NaPO_4$, 300 mM NaCl, and 300 mM imidazole (pH 8.0). Elutions were pooled together and concentrated in a 30K MWCO Amicon Ultra Centrifugal Filter. Concentrated protein was further purified by size exclusion using a HiPrep 16/60 Sephacryl S-300 HR column and 40 mM $NaPO_4$ and 200 mM NaCl (pH 8.0) buffer. The appropriate fractions were pooled and again concentrated in a 30 kDa MWCO Amicon Ultra Centrifugal Filter. Purity was evaluated by SDS-PAGE followed by Coomassie staining.

Obtaining mSA

Monomeric mSA was made by cleaving the MBP tag from Ni-NTA-purified mSA-MBP using TEV protease. The concentration of pooled and concentrated Ni-NTA elutions was determined using a Micro BCA Protein Assay Kit (Thermo Fisher Scientific), and buffer exchanged into 40 mM $NaPO_4$, 200 mM NaCl (pH 8.0) with 0.9 mM biotin, 0.5 mM EDTA, and 1 mM DTT using a 30K MWCO Amicon Ultra Centrifugal Filter. The final volume was diluted to 10 mg/mL. His-tagged TEV Protease (Abcam, Cambridge, UK; ab285976) was added to protein at a 1:25 TEV/protein ratio. Cleavage was facilitated by rotation for 36 h at 4°C. Separation of cleaved mSA from MBP can be done by Ni-NTA resin, which retains the His-tagged MBP and allows mSA to flow through. The cleaved sample was diluted to 10 mL in 40 mM $NaPO_4$ and 200 mM NaCl (pH 8.0), and incubated with 6 mL of HisPur Ni-NTA resin under rotation for 2 h at 4°C. The flow-through containing mSA was collected and the resin was washed with an additional 10 mL of 40 mM $NaPO_4$ and 200 mM NaCl (pH 8.0) buffer. Elution with 15 mL of 40 mM $NaPO_4$, 200 mM NaCl, and 500 mM imidazole (pH 8.0) removed both the His-tagged TEV protease and MBP from the resin. Successful cleavage was confirmed by SDS-PAGE, followed by Coomassie staining.

Labeling with AF 488

Both mSA and mSA-MBP were labeled with AF 488. Concentrated proteins were dialyzed into 0.1 M $NaHCO_3$ (pH 8.4) for 24 h and reacted with an 8 times molar excess of AF 488 NHS ester (Lumiprobe, Cockeysville, MD). The reaction mixture was incubated overnight at 4°C in the dark. Unreacted fluorophore was removed by dialyzing the samples against 50 mM $NaPO_4$ and 150 mM NaCl (pH 8.0) for 24 h, using 10K and 7K MWCO Slide-A-Lyzer Dialysis Cassette (Thermo Fisher Scientific) for mSA-MBP and mSA, respectively. Labeling was confirmed by 10% SDS-PAGE and imaged fluorescently before staining protein bands with Coomassie staining (Fig. S1).

Tetrameric SA labeled with Alexa 488 was obtained from Thermo Fisher Scientific, stored at −20°C, and diluted into flow buffer just before use.

Vesicle and microchannel preparation

We procured the lipids 1,2-diphytanoyl-*sn*-glycero-3-phosphocholine (DiphyPC) and 1,2-dioleoyl-*sn*-glycero-3-phosphoethanolamine-*N*-cap biotinyl (bio-DOPE) from Avanti Polar Lipids (Alabaster, AL), and Texas Red 1,2-dipalmitoyl-*sn*-glycero-3-phosphoethanolamine (TXRed-DPPE) from Thermo Fisher Scientific. We purchased Sylgard 184 from Dow (Midland, MI). All other chemicals were obtained from MilliporeSigma. We made giant unilamellar vesicles by electroformation using an established protocol (21). In brief, we mixed DiphyPC/bio-DOPE/TXRed-DPPE at a molar ratio of 79.2:20:0.8, respectively, and spread the mixture on the conductive side of an indium tin oxide-coated slide (Delta Technologies, Loveland, CO). The lipid film was kept under vacuum for 30 min and then hydrated with 200 mM sucrose solution. We electroformed using an AC electric field with 10 Hz frequency and 1.5 V amplitude at 60°C for 1 h, and used samples on the same day they were made. Electroformed vesicles were diluted into a 200 mM glucose solution to aid sedimentation and 5 mM calcium chloride was added immediately before the solution was injected into a prepared microchannel. Calcium ions facilitate the rupture of giant unilamellar vesicle on glass to form discrete supported lipid bilayer patches (22). This lipid composition forms a uniform fluid phase lipid bilayer at room temperature. The biotinylated lipid concentration was higher (20 mol %) than that used in our previous experiments (2 mol %) to compensate for the lower binding efficiency of monomeric avidin constructs relative to commercially obtained SA.

We followed a rigorous cleaning procedure for glass coverslips to ensure surface homogeneity and hydrophilicity, as described previously (18,23).

We made rectangular polydimethylsiloxane microchannels of approximate width 304 μm and height 125 μm. Polydimethylsiloxane microchannels were permanently plasma bonded to a cleaned glass coverslip immediately before use.

Protein binding and imaging

After membrane patches formed inside the channel, we injected flow buffer (100 mM NaCl, 10 mM Tris, and 1 mM EDTA [pH 8]) containing one of the four proteins. We then sealed the channel outlet and allowed the protein to incubate for 5–30 min. Next, we connected the microchannel to a syringe pump (Harvard Apparatus, Holliston, MA) and gently flushed out excess protein using a small flow rate before beginning image acquisition. At high concentrations, protein-protein interactions can influence the measured collective diffusion constant, and proteins can shield each other from flow, significantly lowering the flow force on each protein (24). To avoid these problems, our objective was to use the lowest possible protein surface concentration compatible with fluorescence imaging. We used a method described previously (25) to estimate the approximate protein surface concentration on supported lipid bilayer patches from the ratio of TXRed-DPPE to Alexa 488, AF488, or GFP fluorescence. The resulting estimated protein surface coverage ranged from 0.3 to 5.3%. A persistent challenge was that mSA binding was low (expected since Lim et al. previously found mSA biotin affinity to be significantly lower than that of wild-type SA). Although it is not clear why the mSA binding was lower than that of mSA-GFP and mSA-MPB, it is consistent with our measurements of the construct binding to free biotin by fluorescence anisotropy, which identified a K_b for mSA that was significantly higher than that for the other two constructs and for commercially obtained SA (Fig. S2). Although we adjusted the incubation concentrations and times to match surface coverage as closely as possible, monomer-based construct concentrations were consistently lower than tetramer concentrations (see supporting material for details).

We also modified our preparation protocols to systematically vary the number of biotinylated lipids bound to tetrameric SA. First, we created conditions that favored SA binding to a single lipid: low biotinylated lipid concentration and an excess of SA. Membrane patches contained only 0.1 mol % bio-DOPE and we increased the concentration of SA during the 30 min incubation to 10 nM (from 4.2 pM in the standard conditions). Next, to create a bias for SA bound to two lipids, we included 20 mol % bio-DOPE and 4.2 pM SA for labeling, but allowed only 5 min for SA binding to membrane patches. Excess SA was then flushed out of the microchannel, and we allowed an additional 45 min of incubation time for SA molecules bound to a single lipid to encounter and bind a second one. We then repeated the flow experiments to measure diffusion and hydrodynamic force in each condition.

For each experiment, we observed the flow response of proteins and lipids in 15–20 symmetric patches, observed in at least three separate microchannels. We recorded time-lapse movies using a spinning disk confocal microscope (Intelligent Imaging Innovations, Denver, CO). We recorded lipid and protein fluorescence with a 40× air objective, using at least four different flow rates for each protein construct (Videos S1 and S2). Flow rates were chosen for each protein independently depending on its initial flow response. After ramping to the maximum flow rate, we recorded a movie with the flow turned off. During experiments, all apparatus and materials were at our lab's usual "room temperature," approximately 28°C.

Image analysis

We analyzed movies using custom MATLAB code as described previously (The MathWorks, Natick, MA) (18). In brief, when flow is applied inside the microchannel, proteins bound to biotinylated lipids move downstream resulting in a formation of a concentration gradient in the flow direction (Fig. 2, *A* and *B*). At steady state, the advective and diffusive forces acting on the protein balance each other and an exponential concentration profile $c(x)$ results with

$$c(x) = e^{\left(\frac{-v}{D}\right)x} \tag{1}$$

where v is the drift velocity and D is the diffusion coefficient (Fig. 2 *C*). Since the flow applied was not strong enough to make the bilayer patch itself slide, the TXRed-DPPE signal remained uniform (Fig. 2, *B–D*). We selected a rectangular region of interest spanning the membrane patch for analysis (Fig. 2, *A* and *B*). Over time, protein accumulates at the patch boundaries; since this protein appears to have a different mobility than the protein on the patch interior, patch edges were excluded from the analysis. We used the TXRed-DPPE intensity to normalize the protein fluorescence signal to correct for intensity variations due to shifts in coverslip position or curvature resulting from pressure changes due to flow. By fitting normalized protein intensity to Eq. 1, we obtained the ratio of v/D at each flow rate.

Surface shear stress at the coverslip is higher in the center of a rectangular microchannel than at the edges. We therefore measured the distance from the channel edge to the center of each membrane patch (y), and used this value to calculate the shear stress σ applied at the patch location by a given flow rate Q applied across the channel of known width w and height h, using the expression (26),

$$\sigma = \eta * \frac{6Q}{h^2(w - 0.630h)}\left[1 - 8\pi^2 \sum_{n_{odd}}^{39} \frac{1}{n^2} \frac{\cosh\left(\frac{n\pi y}{h}\right)}{\cosh\left(\frac{n\pi w}{2h}\right)}\right] \tag{2}$$

In all calculations we assume that flow is consistent with a continuum fluid model with nonslip boundary conditions. We measured the diffusion coefficients for proteins in each membrane patch independently by observing the dynamics of relaxation of the concentration gradient after stopping flow (Fig. 2, *E* and *F*), following a previously published method (27). By fitting the time evolution of the first mode amplitude a of the Fourier transformed intensity profile to the equation

$$a(t) = e^{-\left(\frac{D\pi^2}{L^2}\right)t} \tag{3}$$

where L is the diameter of the membrane patch, we obtained the diffusion constant D (Fig. 2 *G*).

We observed that the measured mSA-MBP diffusion constant decreased over time when the experiment was repeated on the same lipid patch, indicating a tendency for the lipid-anchored constructs to aggregate. We therefore measured the diffusion constant for mSA-MBP as quickly as possible after it bound to the membrane patches, using the minimum necessary flow rate. It was also challenging to determine the diffusion constant for mSA due to its low binding efficiency, resulting in larger uncertainty in our measurement than for the other proteins (Fig. S3).

For patches labeled with SA, total fluorescence signal in the region of analysis was independent of flow rate. We observed a steady reduction of the protein fluorescence due to laser light exposure over the course of an experiment (Fig. S4). This suggests that the surface concentration of SA does not change significantly under flow, although we cannot distinguish between photobleaching and slow loss of bound protein. For monomer and monomer-based constructs, loss of protein during the flow experiment is likely to occur more quickly since binding is weaker. However, a gradual reduction in protein surface concentration will not impact our results. We observed variation in surface concentration of protein on different membrane patches within each experimental preparation, but did not see any correlation between surface concentration and measured diffusion constant or hydrodynamic force (for details, see Figs. S5 and S6).

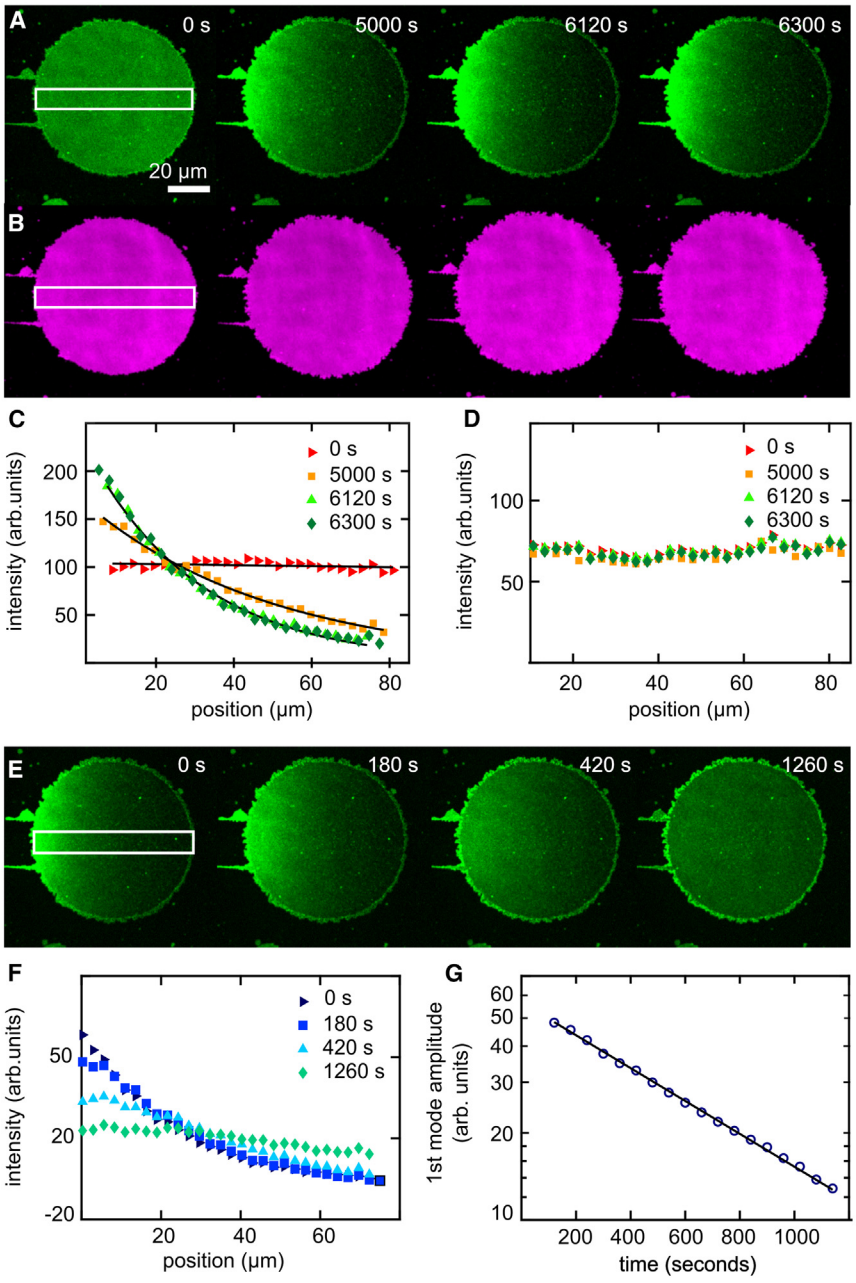

FIGURE 2 Overview of fluorescence gradient method for measuring flow transport. (*A*) When flow is applied, SA (*green*) moves downstream forming a steady-state concentration gradient. A fluorescent lipid marker (TXRed DPPE, *magenta*) is unaffected by flow (*B*). We use the fluorescence intensity inside a rectangle spanning the membrane patch (indicated in *white*) to represent the protein concentration spatial profile at different times during flow for protein (*C*) and lipid (*D*) channels. After flow is turned off, proteins diffuse freely and the gradient relaxes back to a uniform distribution (*E*). We Fourier transform the intensity profile (*F*) and find the diffusion constant by fitting the time evolution of the first mode amplitude to Eq. 3 (*G*).

Simulation setup and protocols

To determine protein shape at the molecular level, we conducted an all-atom molecular dynamics simulation of a lipid-bound mSA. The crystal structure of biotin-bound SA (PDB: 6j6j) (28) was used in combination with a system generated by CHARMM-GUI Membrane Builder (29–32). To match the experiments, the membrane bilayer was composed of DiPhyPC and also contained a single bio-DPPE with an mSA bound to it (Fig. 3 *A*). Advection and diffusion of SA bound to bio-DPPE in DiphyPC membrane patches are indistinguishable from those of SA bound to bio-DOPE (unpublished data). The system was solvated in 0.15 M NaCl and the pressure and temperature were set to 1 bar and 303.15 K, respectively. The initial system size was about $8.9 \times 8.9 \times 11.9$ nm^3 with 198 DiPhyPC and 19,470 water molecules. The CHARMM36m protein and lipid force fields (33–36) and TIP3 water model (37,38) were used. Since there were no force field parameters for bio-DPPE, a bio-DPPE model was parameterized using Antechamber and the general Amber force field (GAFF) (39,40). To properly place the protein above the membrane bilayer, we manipulated the protein through rotation and translation within CHARMM-GUI Membrane Builder STEP 2 (Fig. 3 *B*). The SHAKE algorithm was applied to constrain bond lengths to hydrogen (41), and hydrogen mass repartitioning was utilized to facilitate the simulation with a 4-fs time step (42,43). A force switch distance between 10 and 12 Å was applied to van der Waals interactions. Long-range electrostatic interactions were calculated through the particle-mesh Ewald method (44). According to the default CHARMM-GUI's six-step equilibration protocol (32), a constant particle number, pressure, and temperature ensemble was applied, and the simulation was performed using OpenMM (45) for 1000 ns using the inputs generated by CHARMM-GUI (Fig. 3 *C*, Video S3). (46). We selected a single β strand in the mSA protein, between

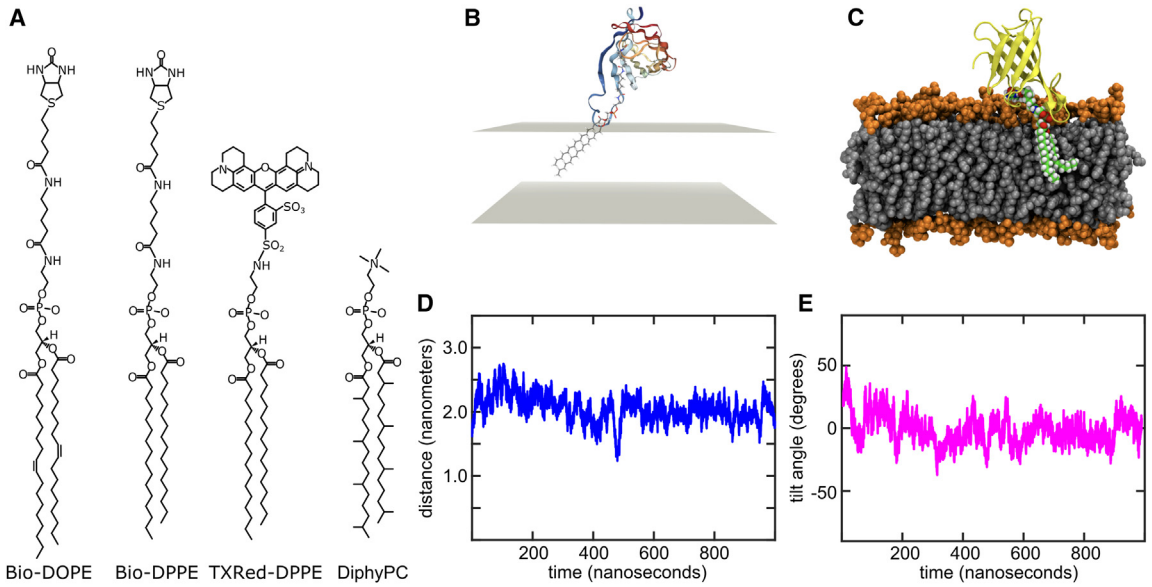

FIGURE 3 Chemical structures and simulation snapshots. (*A*) Structures of lipids used in this experiment (bio-DOPE, DiphyPC, TXRED-DPPE) and in the molecular dynamics simulation (DiPhyPC, bio-DPPE). (*B*) The mSA was oriented relative to the membrane in CHARMM-GUI Membrane Builder STEP 2. (*C*) Snapshot from a molecular dynamics simulation. The protein is displayed in yellow ribbon diagram style. DiPhyPC is represented as spheres with headgroup atoms colored orange and tail atoms colored gray. Bio-DPPE is shown as spheres with carbon atoms colored green, hydrogen atoms white, and oxygen atoms colored red. (*D*) The distance between the z position of the mSA center of mass and the average z position of the upper leaflet lipid phosphate groups. (*E*) The angle between the mSA β barrel axis and a vector normal to the membrane.

residues 124 and 131, and determined the angle between this strand and a vector normal to the lipid membrane. We then subtracted the typical β barrel strand tilt angle, 40°, to obtain the approximate angle between the β barrel axis and the membrane normal (Fig. 3 *E*) (47).

RESULTS

Close to the membrane, the shear rate is approximately linear: the higher a molecule protrudes above the surrounding lipid bilayer, the more force is applied to it by the moving fluid. We expect that the same shear stress will give larger proteins a higher drift velocity than smaller ones. Fig. 4 shows gradients formed by identical shear stress on similarly sized membrane patches decorated with different proteins, demonstrating that this is the case. In our experiments, the applied shear stress is so low (0.1–2 Pa) that it does not induce transport or circulation of lipids in the supported bilayer patch (18). Thus, we observe transport of lipid-anchored proteins relative to lipids that are on average stationary. By combining our measurements of diffusion constant with the concentration gradient slope, we determined the average mobility per Pa of applied shear stress for each protein (Fig. S7). Consistent with our previous experiments, we observe that shear stress induces a temporary, partially reversible increase in the apparent area of our supported bilayer patches (48).

Diffusion constant

Lipid-anchored protein diffusion constants in the absence of flow are primarily determined by membrane viscosity, although fluid drag on the aqueous region of the protein also contributes (49,50). Consistent with this, we found that diffusion constants of SA and mSA-GFP were similar, while mSA diffusion was slightly faster and mSA-MBP diffusion was slower (Table 1; Fig. S8). The simulation revealed that the lower part of the protein was embedded in the membrane headgroups (Fig. 3), which is likely to generate substantial frictional drag. We use the measured diffusion constant (D) to define the *total* viscous drag (f_m). This includes drag applied by the membrane to the lipid anchor and to the lower surface of the protein, as well as drag applied by surrounding fluid to the upper surface of the protein, resulting in the observed diffusion constant $D = k_BT/f_m$.

Lipid anchoring

A single streptavidin molecule comprises four subunits, each of which is primarily formed from a single β barrel. A single biotin binding site is located inside one end of the barrel. In the tetramer, two of the monomers are oriented antiparallel to the other two so that two biotin binding sites are presented on opposite surfaces of the molecule. In our experiment, it is unlikely for all four sites to bind a biotinylated lipid, since this would require creating very high membrane curvature (51). However, it is possible for one or both sites on the same side of a the molecule to bind biotinylated lipids. Our usual preparation protocol results in membrane patches covered primarily with SA that is anchored to the membrane by a single biotinylated lipid

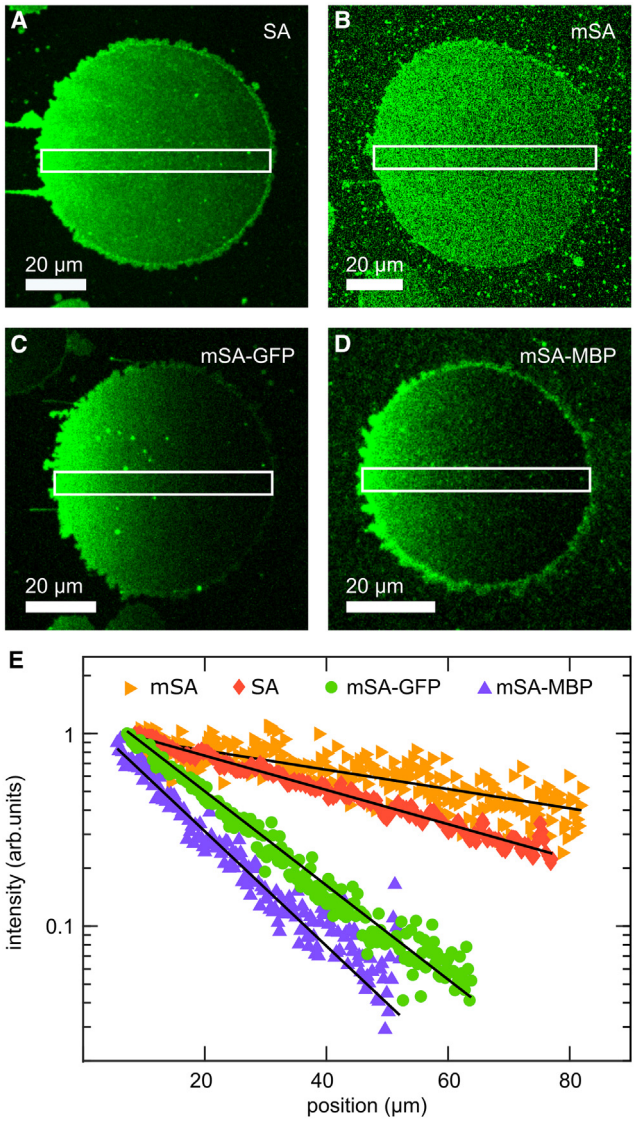

FIGURE 4 Concentration gradients reflect differences in flow-driven transport for different lipid-anchored proteins. (*A–D*) SA, mSA, mSA-GFP, and mSA-MBP form concentration gradients on different membrane patches under approximately 0.5 Pa of shear stress. Flow direction was from right to left in the images. Image contrast was individually adjusted to maximize gradient visibility. mSA-MBP formed the steepest intensity gradient, indicating the highest hydrodynamic force. mSA, the smallest protein, formed the shallowest gradient. (*E*) Normalized and vertically averaged fluorescence intensity as a function of position (fluorescence inside *white rectangles* in *A–D*). Exponential fits (to Eq. 1, with coefficient v/D) are overlaid on each intensity profile.

anchor. To demonstrate this, we modified the preparation procedure to bias the system in favor of single lipid binding by reducing the biotinylated lipid content of the membrane patch to 0.1 mol %, then observed the diffusion constant (Fig. S8 *D*). Under these conditions, we observed a diffusion constant ($1.06 \pm 0.2\ \mu m^2/s$) similar to the one we observed in patches prepared by our usual method ($0.94 \pm 0.17\ \mu m^2/s$). Next, we modified the procedure to favor double lipid binding and observed a significant reduction in the diffusion constant ($0.58 \pm 0.14\ \mu m/s^2$). This represents an increase in the total frictional drag of about 75%. Our results are consistent with previous predictions and observations: in supported membranes, the membrane friction resulting from multiple lipid anchors is predicted to be linearly additive (52). Knight et al. observed that pleckstrin homology domains bound to a single lipid in a supported membrane had a diffusion constant twice as large as domains bound to two lipids (53).

Hydrodynamic force

When the surface concentration of proteins is low, flow applies a constant force to each lipid-anchored protein. The protein reaches a constant terminal "drift velocity" (v) when hydrodynamic force from flow (F_H) balances the total viscous drag (f_m). Due to the boundary conditions imposed by the finite membrane patch, the combined drift velocity and random diffusive motion create a steady-state concentration gradient in the flow direction (Fig. 4 *A–D*). The exponential coefficient of this gradient reflects the ratio v/D, so we obtain the hydrodynamic force directly from this measured coefficient by multiplying it by k_BT. We combined multiple observations for each protein to determine the average hydrodynamic force on an individual protein per Pa of applied shear stress (Fig. 5; Table 1). The results demonstrate that our method applies sub-femtoNewton-sized forces to individual proteins since the surface shear stress we applied ranged between 0.1 and 2.0 Pa.

We note that the average measured force per Pa on mSA was approximately half that on SA. This is consistent with the geometry of these two compact, single-domain molecules since the cross-sectional area of the tetramer should be twice that of the monomer. However, Fig. 5 *B* shows that the hydrodynamic force is not predicted solely by construct molecular weight for the two-domain proteins. Although SA and mSA-GFP have similar molecular weights, the hydrodynamic force on mSA-GFP is more than twice as large as that on SA. This indicates that the hydrodynamic force depends not only on a protein's total molecular weight but also on its folded shape.

DISCUSSION

Protein shape

Previous measurements of flow-mediated mobility of lipid-anchored proteins related the measured protein mobility and hydrodynamic force to the protein's "hydrodynamic area" (A_{hydro}) (16,17). The hydrodynamic area depends both on the cross-sectional area of the protein perpendicular to the flow direction, and on the height of the protein above the bilayer surface. It can be visualized as the area of membrane surface underneath the protein where the flow is disturbed. The hydrodynamic force experienced by a protruding

TABLE 1 Measured and estimated parameters

Protein	Mobility (nm/(Pa.s))	Diffusion (μm^2/s)	Hydrodynamic force (fN/Pa)	No. of membrane patches	Molecular weight (kDa)	Estimated volume (nm^3)
SA	26.3 ± 7.5	0.94 ± 0.17	0.114 ± 0.025	48	52.8	64.0
mSA	19.6 ± 7.3	1.51 ± 0.39	0.054 ± 0.018	40	14.2	17.2
mSA-GFP	50.5 ± 11.4	0.77 ± 0.15	0.26 ± 0.045	47	42.8	51.9
mSA-MBP	64.5 ± 24.7	0.55 ± 0.16	0.48 ± 0.124	52	60.2	73.0

Ranges given are standard deviations.

macromolecule under surface shear stress is linearly related to the hydrodynamic area of that macromolecule, so multiplying the measured F_{hydro} by 1 Pa of surface shear stress yields measured hydrodynamic area of each protein in nm^2 (Fig. 5 *B*). We obtain hydrodynamic area directly from our experiments; but we must make additional approximations to relate the measured area to a particular protein shape.

The detailed shape of a folded protein can be complex, generating a complicated flow interaction that depends on the protein's orientation relative to the flow direction. However, the rotational diffusion constants of individual fluorescent lipids in supported bilayers are on the order of 1×10^6 Hz (54) and unlabeled lipids have similar dynamics (55). Proteins similar in size to mSA diffusing in solution exhibit similarly high rotational diffusion constants (e.g., 1.6×10^7 Hz for lysozyme and 1.9×10^7 Hz for ribonuclease A, respectively (56,57)). If lipid rotation is assumed to be the limiting factor, we can still expect lipid-anchored proteins to rotate on average ≈33 times per second. Protein tilt angle changes on a similar timescale. Since we measure flow-generated concentration gradient slopes over tens of minutes, the hydrodynamic force we measure results from averaging over all likely values of the protein orientation and tilt angle.

The tilt angle and the distance between the protein and the lipid bilayer are thus important parameters for determining the hydrodynamic area of a protein. However, their magnitudes are not immediately obvious from inspection of the crystal structure of folded SA and the molecular structure of the biotinylated lipid (Fig. 3 *A*). We therefore conducted a molecular dynamics simulation of mSA bound to bio-DPPE. The simulation did not include shear flow, since its objective was to determine the typical configuration of a lipid-anchored protein under standard conditions. During the 1 μs simulation, the mSA maintained a position that was close to the membrane and roughly perpendicular to it (Fig. 3 *C*). Over the course of the simulation, the distance between the monomer's center of mass and the surface of the membrane, defined as the average height of the upper leaflet lipid phosphates, was 1.17 ± 0.08 nm (Fig. 3 *D*). This reflects close proximity of the protein to the membrane. In fact, averaging over all time points, 5.7 ± 2.3% of the protein's van der Waals volume was located below the membrane surface. The time-averaged tilt angle was − 1.3 ± 11.7° (Fig. 3 *E*), indicating that the β barrel was perpendicular to the membrane most of the time (Fig. 3 *C*; Video S3). These results suggest that it is reasonable to model mSA using the simple geometric approximation of a cylinder perpendicular to, and in contact with, a flat membrane.

Jönsson and Jönsson modeled hydrodynamic forces on membrane proteins using simplified geometric approximations of protein shape and experimentally confirmed that the surface concentration of membrane proteins modified the hydrodynamic force (24). In the following section, we use their results to quantitatively relate our measured values of A_{hydro} to protein size. Jönsson and Jönsson developed a formula for the hydrodynamic area of a cylindrical molecule, validated by comparing experiments to numerical simulations (24):

$$A_{hydro} = \left[0.65(h_c/r)^2 + 5.0(h_c/r) + 1\right]\pi r^2 \qquad (4)$$

where h_c is the height and r is the radius of the cylinder. This expression describes a cylinder in contact with a flat surface.

We used the measured hydrodynamic areas to generate a "measured cylinder radius" for such cylindrical proteins using Eq. 4 as a function of the ratio of cylinder radius to cylinder height (r/h_c) (Fig. 6, *filled symbols*). Multiple cylinder shapes are compatible with a given hydrodynamic area. To constrain our shape predictions, we calculated the molecular volume of each protein using its known molecular weight (Table 1) and an average value for protein density, 1.37 g/cm^3 (58). This protein volume allowed us to specify an "estimated cylindrical radius" as a function of the radius/height ratio (*open symbols* in Fig. 6). The intersection of the measured radius and estimated radius lines indicates a physically reasonable shape and size estimate. For the compact, single-domain proteins SA and mSA, our measured values of A_{hydro} were consistent with cylinders with r/h_c ratios equal to or greater than one (Fig. 6, *A* and *B*). However, for the two-domain proteins, only taller cylinders yielded a cylinder that was compatible with the total molecular volume: a cylinder at least 4 times taller than its radius in the case of mSA-GFP, or 6 times for mSA-MBP (Fig. 6, *C* and *D*). Taller cylinders are consistent with the shape expected for these two-domain proteins. All parameters obtained for different geometries from the experimental hydrodynamic area and the molecular weight calculations are listed in the supporting material (Tables S4–S7).

Our method yields reasonable estimates for the cylindrical radii: the radius for SA was 3.15 ± 0.4 nm, while the

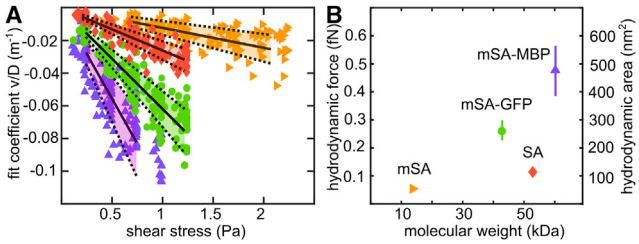

FIGURE 5 Combining multiple measurements yields precise determinations of hydrodynamic force. (*A*) All exponential fit coefficients (v/D) measured for the four proteins at multiple flow rates (converted to shear stress at lower surface of the microchannel) were combined. For each protein, the number of individual membrane patches analyzed is given in Table 1. Solid lines are linear fits, and shaded areas inside dotted lines indicate two standard deviations in slope value. (*B*) Average values of the hydrodynamic force (fN) resulting from 1 Pa of shear stress, with error bars two standard deviations long. The right axis indicates the corresponding value of hydrodynamic area (nm^2) for the four lipid-anchored proteins.

monomer construct radii ranged between 1.6 and 1.7 nm. However, our simple estimate of molecular volume disregards the presence of a "hydration shell" of water molecules closely associated with the protein surface. The impact of a hydration shell on effective protein volume can be significant. For example, the algorithm HullRad predicts hydrated molecular volumes for our small mSA-based constructs that are about 50% larger than the anhydrous volumes (which are similar to our density-based estimates; see Table S3) (57). These hydrated volumes are so large that molecular radius predictions do not intersect with those derived from our measured hydrodynamic areas, as shown in Fig. 6. A possible explanation for this is that the effective size of a protein's hydration shell might be significantly reduced when it is partially embedded in a lipid bilayer, since the membrane and protein hydration shells would have significant overlap. Alternatively, persistent flow might reduce the effective size of a hydration shell by partially dispersing it.

Flow-driven motion of streptavidin

We can quantitatively compare our results for SA with those derived from earlier flow transport experiments. The value we measured for its hydrodynamic area (120 ± 40 nm^2) is smaller than previously reported values of 251 nm^2 by Jönsson and Jönsson (24) and 222 nm^2 by Hu et al. (17) for the same molecule. In both of these previous experiments, high shear stress was applied with the result that the upper leaflet of the bilayer was sliding relative to the lower one at all times. This might result in lower effective membrane drag on proteins and lipids and faster transport by flow, relative to our experiments in which lipids are not flowing (18).

CONCLUSIONS

Advective transport of small particles in moving fluid is described by the Peclet number, the dimensionless ratio of transport rates due to fluid flow and diffusion, respectively. This number is defined as $Pe = \frac{Lv}{D}$, where L is the length scale of interest, v is the velocity due to flow, and D is the diffusion constant. Over protein-sized (nanometer scale) distances, considering protein transport at the drift velocities observed in our experiments yields very small Peclet numbers. For example, we measure the diffusion

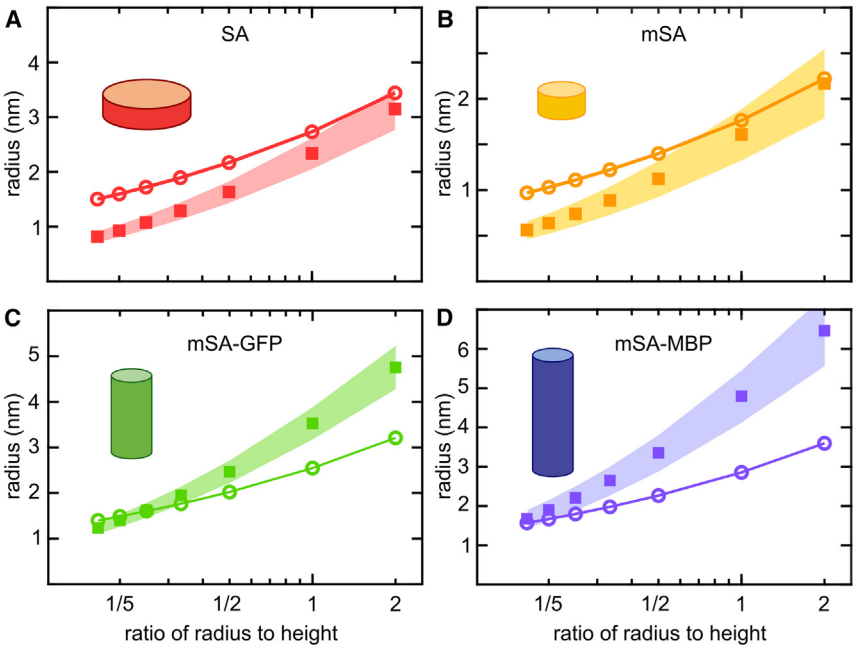

FIGURE 6 Measured cylinder radii as a function of cylinder aspect ratio. (*A–D*) We plot measured cylinder radius against the ratio of radius to height for SA, mSA, mSA-GFP, and mSA-MBP, respectively (*filled squares*; *shaded areas* indicate the radius variation corresponding to two standard deviations in hydrodynamic area). Open circles show the radius required for a cylinder with the given aspect ratio to have the estimated molecular volume. Illustrations showing cylinder shapes are included (with radius to height ratios of 2:1 for SA, 1:1 for mSA, 1:4 for mSA-GFP, and 1:6 for mSA-MBP).

constant for SA to be approximately 1 $\mu m^2/s$, or 1×10^6 nm^2/s. When we apply 1 Pa of shear stress, we observe that its drift velocity is approximately 26 nm/s; considering transport across a distance of 100 nm (about 20 protein widths), the Peclet number is 2.63×10^{-3}. In other words, on nanometer length scales, the impact of flow on protein motion is nearly imperceptible. However, since diffusive motion has no consistent direction, even a small bias in the direction of transport becomes significant when the observation window is expanded to encompass tens of microns, the typical size of our supported membrane patch or of the surface of a single cell. In this case the Peclet number for transport increases, and significant concentration gradients become apparent.

The force required to reshape mechanosensitive proteins has been determined using optical and magnetic tweezers. Proteins such as talin or α actinin can be stretched, typically under forces between 5 and 25 pN, exposing ligand binding sites to function as force sensors (59,60). This degree of stiffness is necessary so that proteins can maintain their structure; otherwise they would be easily deformed by forces arising from thermal noise (in a fluid at 28°C, about 4.3 pN/nm). Individual motor proteins also exert picoNewtons of force: kinesin applies 6.5 pN (61), while myosin generates 1.7 pN of force (62). In our experiment, we applied flows that resulted in less than half a femtoNewton of force to each lipid-anchored protein, an order of magnitude smaller than the forces required to deform them. Therefore, we do not expect the flow forces to cause substantial changes to the protein shape. However, deformation could be achieved by applying larger shear stresses, applying shear stress to larger and more flexible proteins, or applying shear to proteins featuring substantial glycosylation (49). We anticipate that our experimental method can be used to monitor shape changes in these conditions: for example, bending of proteins should result in nonlinear increases in hydrodynamic force at high shear rates.

As previously noted, flow-mediated membrane protein transport provides an alternative method to gel or membrane electrophoresis for membrane protein separation and to study protein-protein interactions (15,16). Since advection by flow depends on protein shape, it could be used to spatially separate multiple conformations of the same protein. In addition, monitoring flow advection allows detection of changes in protein conformation in real time and under conditions similar to physiological ones.

In a recent review, Tanaka et al. note that forces from shear stress due to blood flow are an order of magnitude too small to cause changes in an individual protein's conformation, yet endothelial cells display a variety of robust responses to changes in flow. The identity of the "primary force sensor" in endothelial cells remains unknown (63). Our results demonstrate that the tiny hydrodynamic forces from blood flow are sufficient to generate lateral transport and micron-scale concentration gradients of small lipid-anchored proteins. We speculate that similar flow-driven concentration gradients on cell surfaces may be part of the mechanism of biological flow sensing.

ACKNOWLEDGMENTS

The authors thank Dimitrios Vavylonis and H. Daniel Ou-Yang for helpful discussions. We also thank Yiwei Cao and Sang-Jun Park for assistance with simulation setup. Research in the Honerkamp-Smith and Thévenin labs was supported by the National Institutes of General Medical Studies of the National Institutes of Health under award no. R01GM143320. S.S. was supported in part by a New Investigator Grant from the Charles E. Kaufman Foundation. Research in the Im lab was supported by the Division of Molecular and Cellular Biosciences at the National Science Foundation under award no. MCB-2111728.

AUTHOR CONTRIBUTIONS

S.S. and L. Knepper performed the research, analyzed the data, and wrote the paper. E.A. performed the research and analyzed the data. G.C. analyzed the data and performed the simulations. A.R. performed the research. W.I. and L. Kong performed the simulation and wrote the paper. D.T. and A.H.-S. designed the research and wrote the paper.

DECLARATION OF INTERESTS

The authors declare no competing interests.

SUPPORTING MATERIAL

Supporting material can be found online at https://doi.org/10.1016/j.bpj.2024.08.026.

REFERENCES

1. Paulick, M. G., and C. R. Bertozzi. 2008. The Glycosylphosphatidylinositol Anchor: A Complex Membrane-Anchoring Structure for Proteins. *Biochemistry.* 47:6991–7000. https://doi.org/10.1021/bi8006324.
2. Fujihara, Y., and M. Ikawa. 2016. GPI-AP release in cellular, developmental, and reproductive biology. *J. Lipid Res.* 57:538–545. https://linkinghub.elsevier.com/retrieve/pii/S0022227520354109.
3. Banerjee, T., S. Matsuoka, …, P. A. Iglesias. 2023. A dynamic partitioning mechanism polarizes membrane protein distribution. *Nat. Commun.* 14:7909. https://www.nature.com/articles/s41467-023-43615-2.
4. Ebong, E. E., F. P. Macaluso, …, J. M. Tarbell. 2011. Imaging the Endothelial Glycocalyx In Vitro by Rapid Freezing/Freeze Substitution Transmission Electron Microscopy. *Arterioscler. Thromb. Vasc. Biol.* 31:1908–1915. https://doi.org/10.1161/ATVBAHA.111.225268.
5. Van Den Berg, B. M., J. A. E. Spaan, and H. Vink. 2009. Impaired glycocalyx barrier properties contribute to enhanced intimal low-density lipoprotein accumulation at the carotid artery bifurcation in mice. *Pflügers Archiv.* 457:1199–1206. https://doi.org/10.1007/s00424-008-0590-6.
6. Dai, G., M. R. Kaazempur-Mofrad, …, M. A. Gimbrone, Jr. 2004. Distinct endothelial phenotypes evoked by arterial waveforms derived from atherosclerosis-susceptible and -resistant regions of human vasculature. *Proc. Natl. Acad. Sci. USA.* 101:14871–14876.
7. Beurskens, D. M., M. E. Bol, …, J.-W. E. Sels. 2020. Decreased endothelial glycocalyx thickness is an early predictor of mortality in sepsis.

Anaesth. Intensive Care. 48:221–228. https://doi.org/10.1177/0310057X20916471.

8. Dong, C., Y. K. Choi, …, W. Im. 2021. Structure, Dynamics, and Interactions of GPI-Anchored Human Glypican-1 with Heparan Sulfates in a Membrane. *Glycobiology.* 31:593–602. https://academic.oup.com/glycob/article/31/5/593/5918341.
9. Ohi, M. D., and A. K. Kenworthy. 2022. Emerging Insights into the Molecular Architecture of Caveolin-1. *J. Membr. Biol.* 255:375–383. https://doi.org/10.1007/s00232-022-00259-5.
10. Tao, X., C. Zhao, and R. MacKinnon. 2023. Membrane protein isolation and structure determination in cell-derived membrane vesicles. *Proc. Natl. Acad. Sci. USA.* 120:e2302325120. https://doi.org/10.1073/pnas.2302325120.
11. Groves, J. T., and S. G. Boxer. 1995. Electric field-induced concentration gradients in planar supported bilayers. *Biophys. J.* 69:1972–1975. https://linkinghub.elsevier.com/retrieve/pii/S0006349595800676.
12. Liu, C., C. F. Monson, …, P. S. Cremer. 2011. Protein Separation by Electrophoretic–Electroosmotic Focusing on Supported Lipid Bilayers. *Anal. Chem.* 83:7876–7880. https://doi.org/10.1021/ac201768k.
13. Huang, S.-H., B.-C. Huang, and L. Chao. 2022. Development of Cell Membrane Electrophoresis to Measure the Diffusivity of a Native Transmembrane Protein. *Anal. Chem.* 94:4531–4537. https://doi.org/10.1021/acs.analchem.2c00211.
14. Engstler, M., T. Pfohl, …, P. Overath. 2007. Hydrodynamic Flow-Mediated Protein Sorting on the Cell Surface of Trypanosomes. *Cell.* 131:505–515. https://linkinghub.elsevier.com/retrieve/pii/S0092867407011440.
15. Jönsson, P., A. Gunnarsson, and F. Höök. 2011. Accumulation and Separation of Membrane-Bound Proteins Using Hydrodynamic Forces. *Anal. Chem.* 83:604–611. https://doi.org/10.1021/ac102979b.
16. Jonsson, P., J. McColl, …, D. Klenerman. 2012. Hydrodynamic trapping of molecules in lipid bilayers. *Proc. Natl. Acad. Sci. USA.* 109:10328–10333. https://doi.org/10.1073/pnas.1202858109.
17. Hu, S.-K., L.-T. Huang, and L. Chao. 2016. Membrane species mobility under in-lipid-membrane forced convection. *Soft Matter.* 12:6954–6963. http://xlink.rsc.org/?DOI=C6SM01145D.
18. Ratajczak, A. M., S. Sasidharan, A. R. Honerkamp-Smith…, 2023. Measuring flow-mediated protein drift across stationary supported lipid bilayers. *Biophys. J.* 122:1720–1731.
19. Lim, K. H., H. Huang, …, S. Park. 2013. Stable, high-affinity streptavidin monomer for protein labeling and monovalent biotin detection. *Biotechnol. Bioeng.* 110:57–67. https://doi.org/10.1002/bit.24605.
20. Lim, K. H., H. Huang, …, S. Park. 2011. Engineered Streptavidin Monomer and Dimer with Improved Stability and Function. *Biochemistry.* 50:8682–8691. https://doi.org/10.1021/bi2010366.
21. Angelova, M. I., S. Soléau, …, P. Bothorel. 1992. Preparation of giant vesicles by external AC electric fields. Kinetics and applications. *In* Trends in Colloid and Interface Science VI, *89*. C. Helm, M. Lösche, and H. Möhwald, eds. Steinkopff, Darmstadt, pp. 127–131. series Title: Progress in Colloid & Polymer Science. https://doi.org/10.1007/BFb0116295.
22. Seelig, J. 1990. Interaction of phospholipids with Ca2+ Ions. On the role of the phosopholipid head groups. *Cell Biol. Int. Rep.* 14:353–360.
23. Chada, N., K. P. Sigdel, …, G. M. King. 2015. Glass is a Viable Substrate for Precision Force Microscopy of Membrane Proteins. *Sci. Rep.* 5:12550. http://www.nature.com/articles/srep12550.
24. Jönsson, P., and B. Jönsson. 2015. Hydrodynamic Forces on Macromolecules Protruding from Lipid Bilayers Due to External Liquid Flows. *Langmuir.* 31:12708–12718. https://doi.org/10.1021/acs.langmuir.5b03421.
25. Galush, W. J., J. A. Nye, and J. T. Groves. 2008. Quantitative Fluorescence Microscopy Using Supported Lipid Bilayer Standards. *Biophys. J.* 95:2512–2519. https://linkinghub.elsevier.com/retrieve/pii/S0006349508783954.
26. Jönsson, P., J. P. Beech, …, F. Höök. 2009. Mechanical Behavior of a Supported Lipid Bilayer under External Shear Forces. *Langmuir.* 25:6279–6286. https://doi.org/10.1021/la8042268.
27. Zhang, H.-Y., and R. J. Hill. 2011. Lipopolymer gradient diffusion in supported bilayer membranes. *J. R. Soc. Interface.* 8:312–321. https://doi.org/10.1098/rsif.2010.0352.
28. Fan, X., J. Wang, …, H.-W. Wang. 2019. Single particle cryo-EM reconstruction of 52 kDa streptavidin at 3.2 Angstrom resolution. *Nat. Commun.* 10:2386. https://www.nature.com/articles/s41467-019-10368-w.
29. Wu, E. L., X. Cheng, …, W. Im. 2014. CHARMM-GUI *Membrane Builder* toward realistic biological membrane simulations. *J. Comput. Chem.* 35:1997–2004. https://doi.org/10.1002/jcc.23702.
30. Feng, S., S. Park, …, W. Im. 2023. CHARMM-GUI *Membrane Builder* : Past, Current, and Future Developments and Applications. *J. Chem. Theor. Comput.* 19:2161–2185. https://doi.org/10.1021/acs.jctc.2c01246.
31. Jo, S., T. Kim, …, W. Im. 2008. CHARMM-GUI: A web-based graphical user interface for CHARMM. *J. Comput. Chem.* 29:1859–1865. https://doi.org/10.1002/jcc.20945.
32. Jo, S., T. Kim, and W. Im. 2007. Automated Builder and Database of Protein/Membrane Complexes for Molecular Dynamics Simulations. *PLoS One.* 2:e880. https://doi.org/10.1371/journal.pone.0000880.
33. Huang, J., S. Rauscher, …, A. D. MacKerell, Jr. 2017. CHARMM36m: an improved force field for folded and intrinsically disordered proteins. *Nat. Methods.* 14:71–73.
34. Klauda, J. B., R. M. Venable, …, R. W. Pastor. 2010. Update of the CHARMM All-Atom Additive Force Field for Lipids: Validation on Six Lipid Types. *J. Phys. Chem. B.* 114:7830–7843. https://doi.org/10.1021/jp101759q.
35. Huang, J., and A. D. MacKerell. 2013. CHARMM36 all-atom additive protein force field: Validation based on comparison to NMR data. *J. Comput. Chem.* 34:2135–2145. https://doi.org/10.1002/jcc.23354.
36. Best, R. B., X. Zhu, …, A. D. MacKerell. 2012. Optimization of the Additive CHARMM All-Atom Protein Force Field Targeting Improved Sampling of the Backbone \textphi, \textpsi, and \textchi1 and \textchi2 Dihedral Angles. *J. Chem. Theor. Comput.* 8:3257–3273.
37. Jorgensen, W. L., J. Chandrasekhar, …, M. L. Klein. 1983. Comparison of simple potential functions for simulating liquid water. *J. Chem. Phys.* 79:926–935. https://pubs.aip.org/jcp/article/79/2/926/776316/Comparison-of-simple-potential-functions-for.
38. Durell, S. R., B. R. Brooks, and A. Ben-Naim. 1994. Solvent-Induced Forces between Two Hydrophilic Groups. *J. Phys. Chem.* 98:2198–2202. https://doi.org/10.1021/j100059a038.
39. Wang, J., W. Wang, …, D. A. Case. 2006. Automatic atom type and bond type perception in molecular mechanical calculations. *J. Mol. Graph. Model.* 25:247–260. https://linkinghub.elsevier.com/retrieve/pii/S1093326305001737.
40. Wang, J., R. M. Wolf, …, D. A. Case. 2004. Development and Testing of a General Amber Force Field. *J. Comput. Chem.* 25:1157–1174. https://doi.org/10.1002/jcc.20035.
41. Ryckaert, J.-P., G. Ciccotti, and H. J. C. Berendsen. 1977. Numerical Integration of the Cartesian Equations of Motion of a System with Constraints: Molecular Dynamics of n-Alkanes. *J. Comput. Phys.* 23:327–341.
42. Gao, Y., J. Lee, …, W. Im. 2021. CHARMM-GUI Supports Hydrogen Mass Repartitioning and Different Protonation States of Phosphates in Lipopolysaccharides. *J. Chem. Inf. Model.* 61:831–839. https://doi.org/10.1021/acs.jcim.0c01360.
43. Hopkins, C. W., S. Le Grand, …, A. E. Roitberg. 2015. Long-Time-Step Molecular Dynamics through Hydrogen Mass Repartitioning. *J. Chem. Theor. Comput.* 11:1864–1874. https://doi.org/10.1021/ct5010406.
44. Darden, T., D. York, and L. Pedersen. 1993. Particle mesh Ewald: An N log(N) method for Ewald sums in large systems. *J. Chem. Phys.* 98:10089–10092. https://pubs.aip.org/jcp/article/98/12/10089/461765/Particle-mesh-Ewald-An-N-log-N-method-for-Ewald.
45. Eastman, P., J. Swails, …, V. S. Pande. 2017. OpenMM 7: Rapid development of high performance algorithms for molecular dynamics. *PLoS Comput. Biol.* 13:e1005659. https://doi.org/10.1371/journal.pcbi.1005659.

46. Lee, J., X. Cheng, …, W. Im. 2016. CHARMM-GUI Input Generator for NAMD, GROMACS, AMBER, OpenMM, and CHARMM/OpenMM Simulations Using the CHARMM36 Additive Force Field. *J. Chem. Theor. Comput.* 12:405–413. https://doi.org/10.1021/acs.jctc.5b00935.

47. Páli, T., and D. Marsh. 2001. Tilt, Twist, and Coiling in \textbeta-Barrel Membrane Proteins: Relation to Infrared Dichroism. *Biophys. J.* 80:2789–2797.

48. Miller, E. J., M. D. Phan, …, A. R. Honerkamp-Smith. 2023. Passive and reversible area regulation of supported lipid bilayers in response to fluid flow. *Biophys. J.* 122:2242–2255. https://linkinghub.elsevier.com/retrieve/pii/S0006349523000280.

49. Gurdap, C. O., L. Wedemann, …, E. Sezgin. 2022. Influence of the extracellular domain size on the dynamic behavior of membrane proteins. *Biophys. J.* 121:3826–3836. https://linkinghub.elsevier.com/retrieve/pii/S0006349522007603.

50. Liao, Y.-H., C.-H. Lin, …, C.-L. Hsieh. 2019. Monovalent and Oriented Labeling of Gold Nanoprobes for the High-Resolution Tracking of a Single-Membrane Molecule. *ACS Nano.* 13:10918–10928. https://doi.org/10.1021/acsnano.9b01176.

51. Yamamoto, D., N. Nagura, …, T. Ando. 2009. Streptavidin 2D Crystal Substrates for Visualizing Biomolecular Processes by Atomic Force Microscopy. *Biophys. J.* 97:2358–2367. https://linkinghub.elsevier.com/retrieve/pii/S0006349509013095.

52. Camley, B. A., and F. L. H. Brown. 2019. Motion of objects embedded in lipid bilayer membranes: Advection and effective viscosity. *J. Chem. Phys.* 151:124104. https://doi.org/10.1063/1.5121418.

53. Knight, J. D., M. G. Lerner, …, J. J. Falke. 2010. Single Molecule Diffusion of Membrane-Bound Proteins: Window into Lipid Contacts and Bilayer Dynamics. *Biophys. J.* 99:2879–2887. https://linkinghub.elsevier.com/retrieve/pii/S0006349510010428.

54. Harms, G. S., M. Sonnleitner, …, T. Schmidt. 1999. Single-Molecule Anisotropy Imaging. *Biophys. J.* 77:2864–2870. https://linkinghub.elsevier.com/retrieve/pii/S0006349599771183.

55. Shin, Y. K., and J. H. Freed. 1989. Dynamic imaging of lateral diffusion by electron spin resonance and study of rotational dynamics in model membranes. Effect of cholesterol. *Biophys. J.* 55:537–550. https://linkinghub.elsevier.com/retrieve/pii/S0006349589828474.

56. Rai, N., M. Nöllmann, …, M. Rocco. 2005. SOMO (SOlution MOdeler). *Structure.* 13:723–734. https://linkinghub.elsevier.com/retrieve/pii/S0969212605001164.

57. Fleming, P. J., and K. G. Fleming. 2018. HullRad: Fast Calculations of Folded and Disordered Protein and Nucleic Acid Hydrodynamic Properties. *Biophys. J.* 114:856–869. https://linkinghub.elsevier.com/retrieve/pii/S0006349518300651.

58. Erickson, H. P. 2009. Size and Shape of Protein Molecules at the Nanometer Level Determined by Sedimentation, Gel Filtration, and Electron Microscopy. *Biol. Proced. Online.* 11:32–51. http://www.biologicalproceduresonline.com/content/11/1/32.

59. Yao, M., B. T. Goult, …, J. Yan. 2014. Mechanical activation of vinculin binding to talin locks talin in an unfolded conformation. *Sci. Rep.* 4:4610. https://www.nature.com/articles/srep04610.

60. Le, S., X. Hu, …, J. Yan. 2017. Mechanotransmission and Mechanosensing of Human alpha-Actinin 1. *Cell Rep.* 21:2714–2723. https://linkinghub.elsevier.com/retrieve/pii/S2211124717316777.

61. Visscher, K., M. J. Schnitzer, and S. M. Block. 1999. Single kinesin molecules studied with a molecular force clamp. *Nature.* 400:184–189. https://www.nature.com/articles/22146.

62. Molloy, J. E., J. E. Burns, …, D. C. White. 1995. Movement and force produced by a single myosin head. *Nature.* 378:209–212. https://www.nature.com/articles/378209a0.

63. Tanaka, K., D. Joshi, …, M. A. Schwartz. 2021. Early events in endothelial flow sensing. *Cytoskeleton.* 78:217–231. https://doi.org/10.1002/cm.21652.